IEEE Access
Multidisciplinary | Rapid Review | Open Access Journal

Date of publication xxxx 00, 0000, date of current version xxxx 00, 0000.

Digital Object Identifier 10.1109/ACCESS.2017.Doi Number

Potential Visible-light Driven PtO_2/GaN vdW Hetero-bilayer Photocatalysts for Water Splitting using First-principles

MD. SAKIB HASAN KHAN[1], MUHAMMAD SHAFFATUL ISLAM[2], MD. RAFIQUL ISLAM[1], SENIOR MEMBER, IEEE, AHAMED ISKANDERANI[3], IBRAHIM M. MEHEDI[3,4], and MD. TANVIR HASAN[5], SENIOR MEMBER, IEEE

[1]Department of Electrical and Electronic Engineering (EEE), Khulna University of Engineering & Technology (KUET), Khulna-9203, Bangladesh
[2]Department of Electrical and Electronic Engineering (EEE), World University of Bangladesh (WUB), Dhaka-1205, Bangladesh
[3]Department of Electrical and Computer Engineering (ECE), King Abdulaziz University, Jeddah 21589, Saudi Arabia
[4]Center of Excellence in Intelligent Engineering Systems (CEIES), King Abdulaziz University, Jeddah 21589, Saudi Arabia
[5]Department of Electrical and Electronic Engineering (EEE), Jashore University of Science and Technology (JUST), Jashore-7408, Bangladesh

Corresponding author: Md. Tanvir Hasan (e-mail: tan_vir_bd@yahoo.com).

This work was supported by the Deanship of Scientific Research (DSR), King Abdulaziz University, Jeddah, under grant No. (DF 755-135-1441).

ABSTRACT Novel two-dimensional (2D) PtO_2/GaN van der Waals (vdW) hetero-bilayers (HBL) are studied here for photocatalytic water splitting (PWS) application under first-principles density functional theory (DFT). We proposed six HBLs due to the atomic orientational variations and two of them are found dynamically stable confirmed by phonon dispersion curves. The two stable HBLs, HBL1, and HBL6 also show negative binding energy depicted by the interlayer distance-dependent binding energy curves. Among them, HBL1 has the lowest binding energy, suggesting the exothermic practicability of the material. Electronically both materials show a visible ranged indirect bandgap of ~2.65 (2.69) eV for HBL 1 (HBL6), lowered by ~2 times compared to their intrinsic constituents (2D PtO_2, 2D GaN). The bandgaps also have type-II band orientation, which is highly required for efficient spatial carrier separation in photocatalytic water splitting (PWS) applications. The optical properties of the HBLs were also calculated, and it's found that the HBLs have ~2×10^5 cm^{-1} of perovskite material-like absorption coefficient in the visible spectrum, a key requirement for efficient photocatalysis. Reflectivity is as low as ~7 % in the visible spectrum, suggesting the low-loss nature of the materials. Photocatalytic band-edges with type-II band alignments show sufficient kinetic overpotential for hydrogen evolution reaction (HER) and oxygen evolution reaction (OER) in both HBLs, suggesting effective water-splitting capacity. Moreover, we have explored the biaxial strain-induced tunability of the electronic bandgap, absorption coefficients, and photocatalytic band edges. They all found responsive due to homogeneous biaxial strain and show bandgap-lowering, absorption coefficient visible shifting, and band-edges tuning from compressive to tensile strains in the -6 % to +6% range. These studies suggest that the novel PtO_2/GaN vdW layered material can be a probable efficient material for visible-light-driven photocatalytic water-splitting technology.

INDEX TERMS 2D PtO_2/GaN, hetero-bilayer, Van der Waals (vdW) concept, first-principles density functional theory (DFT), optoelectronic property, photocatalytic water splitting.

I. INTRODUCTION

The incremental energy consumption is made globally, causing a detrimental environmental effect as the energy sources are mainly from fossil fuels [1]. This leads to CO_2 emission worldwide to the extent that was never before, resulting in serious global warming [2], [3]. An energy alternative, potentially high-efficient, renewable, and facilitated by low- or zero CO_2 -emission is highly demanding to reduce this negative effect. This leads to an eloquently simple concept of hydrogen (H_2) fuel production from water using a semiconductor-based splitting mechanism [4], [5]. The core attractiveness of the concept is that harnessing the two-

This article has been accepted for publication in a future issue of this journal, but has not been fully edited. Content may change prior to final publication. Citation information: DOI 10.1109/ACCESS.2021.3102190, IEEE Access

dimensional (2D) semiconductor and layered materials-based photocatalysts, the water can be split into oxygen (O_2) and H_2 with zero CO_2-emission while the traditional biomass-gasification process of H_2 fuel production comes up with CO_2 byproduct [6]. However, finding an efficient photocatalyst is on the search, and many scientists are exploring newer and newer possibilities. In this regard, the key challenge is to seek a material having all the attributes for photocatalytic water splitting (PWS). The attributes are the following: the material must possess (i) suitable bandgap (~1.23 eV) and band-edges so that the kinetic overpotential become sufficient for hydrolysis, (ii) spatial carrier separation capability and high-surface to volume ratio so that photocatalytic sites can be increased, and (iii) high-optical absorption in the visible or near ultra-violet (NUV) spectrum so that the peak solar irradiations can be utilized. To acquire these features, nanostructured 2D materials are the best candidates as they have suitable band-gap, high-surface to volume ratio, superior carrier mobility, and considerable absorption co-efficient [5], [7]–[9]. The prominent proof regarding it is the first nanostructured (nanoparticle) photocatalysts, TiO_2 outperforms in water splitting with better hydrogen yield than its bulk structure [7], [10]. From this evidences, many 2D materials are coming into the light for PWS application. Among them, a nonmetallic graphene-like C_3N_4 shows ~ 3.2 μmol/h/g of H_2 production at ~ $\lambda > 420$ nm visible lights with ~10 m^2/g surface area and ~ 2.7 eV near-ultraviolet (NUV) bandgap [9], [11]. It shows almost by ~35 (~106 μmol/h/g) times more yields when Pt co-catalysts are added. Bandgap engineered graphene outperforms in this respect almost by ~100 (~1050 μmol/h/g) times more yields than the previous one [5]. Besides, 2D transition metal dichalcogenides (TMDs) show a tangible change (~26000, ~62000, and ~2580 μmol/h/g of yields for MoS_2, $MoSe_2$, and WS_2, correspondingly) in H_2 yields using their self-polarizing properties [5], [12], [13]. However, the spatial carrier separation, another key requirement for PWS cannot be acquired by only 2D materials. Here, comes another alluring concept, vdW stacked layered materials, as with the properties like 2D materials, they also have bandgap tunability due to stacking patterns, spatial carrier separation capability, and superior optical absorption [14], [15]. With the advent of nanotechnology, emergent materials, precisely, graphene, 2D oxides, 2D transition metals dichalcogenides (TMDs), and 2D group III-V are experimentally realized and unleashed the astonishingly unique properties of the materials [12], [16], [17]. As such material is 2D PtO_2, having superior thermo-mechanical stability with ~175.78 N/m of mechanical stiffness, two valley bandgap of ~1.67 eV (PBE), ~3.15 eV (HSE06), and ~3.59 eV (GW), superior optical absorption and carrier mobility, is numerously used as substrate material for many-layered materials, hetero-bilayers for photovoltaics and PWS applications [18]. For example, ZnO/PtO_2 vdW hetero-bilayer (HBL), with direct type-II 0.47 eV of bandgap, can be used in photodetector application [19], PtO_2/MoS_2 vdW HBL with indirect bandgap shows photocatalysis property [20], experimentally synthesized $Ni(OH)_2/PtO_2$ nanostructured array show enhanced hydrogen evolution reaction (HER) [21], and PtO_2 based nanoparticle show improved HER [22]. Besides, the PtO_2 based 2D and vdW structures show altering bandgap, enhanced HER, and improved optical absorption. Another promising 2D material, 2D planar GaN with a large ultraviolet (UV) ranged bandgap ~4.42 eV (GW), and ~4.18 eV-5.2 eV (experimental) bandgap, high thermal and chemical stability, mechanically robustness (~108.37 mechanical stiffness and 0.410 Poisson's ratio), self-polarizing capability, and ultra-high carrier mobility makes it available in wide ranges of application namely, photovoltaics, coating material, UV-detector, and dielectric material for nano-transistors [23]–[26]. It is also experimentally realized [24], [27]. Moreover, the vdW concept of 2D GaN is widely used as direct-Z scheme type-II bandgap photocatalysts for water splitting [15], [28]–[30]. Some of the shreds of evidence are compiled in **TABLE I**. Among them, 2D GaN stacked with TMDs, and transition metal oxides (TMO) outperforms due to their visible driven PWS capability with cross-plane spatial carrier separation (SCS). Besides, MoS_2/GaN, phosphorene/GaN, GeC/GaN, BAs/GaN, and BP/GaN are all show tunable electronic, optical properties with tunable PWS band edges due to stacking variations and external perturbation (biaxial strain, and cross-plane electric field) [29], [31]–[33].

TABLE I
2D GaN AND PtO_2 BASED vdW STRUCTURES IN LITERATURE AS PHOTOCATALYSTS

Materials	E_g (eV)	Remarks	Ref.
ZnO/GaN	2.82-D	Type-II, tunability absent	[34], [35]
GaN/GeC	3.47 (MGGA), D	Type-II, tunability present	[15]
GaN/MoSe2	1.65-1.7(HSE06), I	Type-II, tunability present	[31]
GaN/WSe2	1.7-1.8 (HSE06), D	Type-II, tunability present(slight)	[31]
GaN/BAs	1.7(HSE06), D	Type-II, tunability absent	[28]
MoSSe/GaN	1.5 (HSE06), D	Type-II, tunability absent	[29]
BP/GaN	1.6 (HSE06). D, I	Type-II, tunability present	[36]
PtO_2/MoS_2	1.5 (HSE06), I	Type-II, tunability absent	[20]

D = direct bandgap, I = indirect bandgap

This article has been accepted for publication in a future issue of this journal, but has not been fully edited. Content may change prior to final publication. Citation information: DOI 10.1109/ACCESS.2021.3102190, IEEE Access

However, to our best knowledge, the vdW PtO_2/GaN hetero-bilayer is not studied yet for the PWS application, though 2D PtO_2 and 2D GaN possess astounding intrinsic and tunable optoelectronic properties. Therefore, in this study, we have introduced the novel vdW PtO_2/GaN hetero-bilayer with all of its stacking variants and explore the PWS attributes of the materials. Also, to unlock tunability in electronic, optical, and photocatalytic properties, biaxial strain is introduced. These studies suggest that the novel vdW PtO_2/GaN hetero-bilayer, with visible ranged bandgap, high-optical absorption, and tunable photocatalytic properties can be a promising material for advanced PWS technology.

II. COMPUTATIONAL METHODOLOGY

For the density functional theory (DFT) calculations, **C**ambridge **S**erial **T**otal **E**nergy **P**ackage (CASTEP), an academic opensource version, is used which utilizes a plane-wave basis set [37]. Electron-ion interactions are described by the norm-conserving pseudopotential (NCP). To predict electronic properties, we initially implemented Perdew-Burke-Erzernhof (PBE) functional with generalized gradient approximation (GGA) exchange-correlation [38]. Conventionally, GGA-PBE exchange-correlation functional predict bandgap underestimated from experimental bandgap of a semiconductor. Heyd-Scusena-Ernzerhof's (HSE 06) nonlocal hybrid functional was introduced to minimize the bandgap problem [39]. Besides, customized meta-GGA (MGGA) functional with 2D PRHG with regularized PBE is utilized to further reduce the deviation between theoretical and experimental bandgap [40]. We have also evaluated the predicted bandgap value with experimental and quasi-particle (QP) bandgap values. The vdW interaction, significant in the stacked HBLs, is defined by semi-empirical Grimme dispersion corrected density functional theory (DFT-D3) [41]. To model the vdW stacked HBLs, a 2×2 supercell of 2D PtO_2 and 2D GaN are chosen and oriented in six different ways. For each 2D layer, a 30 Å vacuum slab model is used.

For structural relaxation Broyden-Fletcher-Goldfarb-Shanno (BFGS) algorithm is used with energy cut-off 800 eV. The energy, stress, force, and displacement tolerance cutoff are 1×10^{-5} eV/atom, 0.05 GPa, 0.03 eV/Å, and 0.001 Å, correspondingly. The K- points sampling for reciprocal space are 9 × 9 ×1, 15 × 15 ×1, and 30 × 30 × 1 for electronic band structure, projected density of states (PDOS), and optical properties calculations, respectively. For predicting the exothermic feasibility of the stacking, the binding energy is introduced equated by the following equation,

$$E_b = \left[E_{heterobilayer} - \sum_i E_i(layer_i)\right] \quad (1)$$

where, $E_{heterobilayer}$ is the dispersion corrected total energy of the hetero-bilayer system, and $\sum_i E_i(layer_i)$ is the sum of the energies of i numbers of 2D layers for stacking the hetero-bilayer. Likewise, the formula used for charge density difference calculation is the following,

$$\Delta\rho = \rho_{hetrobilayer} - \sum_i \rho_i(layer) \quad (2)$$

here, $\rho_{hetrobilayer}$ is the vdW HBL's charge density and $\sum_i \rho_i(layer)$ is the accumulated charge density of the 2D layer used for vdW stacking. Besides, to predict the dynamical stability of the HBLs, density functional perturbation theory (DFPT) initiated phonon dispersion curves are introduced.

For strain-dependent tunability of the properties, the following equation is applied,

$$a_s = \pm e \times a_u + a_u \quad (3)$$

where, a_s and a_u denotes strained and unstrained lattice constants, correspondingly. The e with +ve (-ve) sign signifies the tensile (compressive) strains.

For calculating density functional theory (DFT) based dielectric function, $\varepsilon(\omega) = \varepsilon_1(\omega) + i\varepsilon_2(\omega)$, the complex dielectric constant is evaluated first. Interestingly, a singularity between inter-band transition energies and complex dielectric function is found evaluated by [42], [43],

$$\varepsilon_2 = \frac{2e^2\pi}{\Omega\varepsilon_0} \sum_{k,v,c} |\langle\psi_k^c|\hat{u} \times r|\psi_k^v\rangle|^2 \delta(E_k^c - E_k^v - E) \quad (4)$$

where, e = electronic charge, $\hat{u}$ = vector defining the polarization of incident filed, Ω = polarization density, r = spatial position, ψ_k^c and ψ_k^v = the conduction band (CB) and valence band (VB) wave-function at k respectively. E_k^c = the conduction band energy, E_k^v = valance band energy, and E = Fermi energy.

III. RESULTS AND DISCUSSION

A. STRUCTURAL PROPERTIES

We have first included here the structural details of our proposed PtO_2/GaN vdW HBLs along with the constituents. The 2D GaN (α-PtO_2) is planar (buckling) with a hexagonal structure (P-3M1). The calculated lattice parameters for 2D α-PtO_2 (GaN) are the following: lattice constant, a ~ 3.168 (3.248) Å, bond length, d_B ~ 2.07 (1.875) Å, and buckling height, d_H ~ 1.865 (0.0) Å. These lattice parameters are well-aligned with other theoretical and experimental studies [18], [44]–[47][26], [31], [42]. For stacking the 2D layers, 2D PtO_2 (α-phase) is assumed as substrate layer and 2D GaN is vertically placed on top of that layer. While stacking, lattice mismatch arises due to the lattice constant discrepancy of the 2D layers and the mismatch is ~ 2.5 %, quite lower compared with other vdW stacked HBLs, as calculated by $\%mismatch = 100\ (a_{2D\ GaN} - a_{2D\ PtO2})/a_{2D\ PtO2}$ [15], [19], [28], [34]. This mismatch value is also in the allowable value (below 5%) of the vdW stacking, suggesting the possibility of stacking. The six variants of the HBLs are oriented in the following manner: First, we defined two oxygen atoms in the buckling structure of PtO_2 as upper oxygen (O_u) and lower oxygen (O_l). Now, in HBL 1, gallium (Ga) and nitrogen (N) atoms stacked on top of platinum (Pt)

This article has been accepted for publication in a future issue of this journal, but has not been fully edited. Content may change prior to final publication. Citation information: DOI 10.1109/ACCESS.2021.3102190, IEEE Access

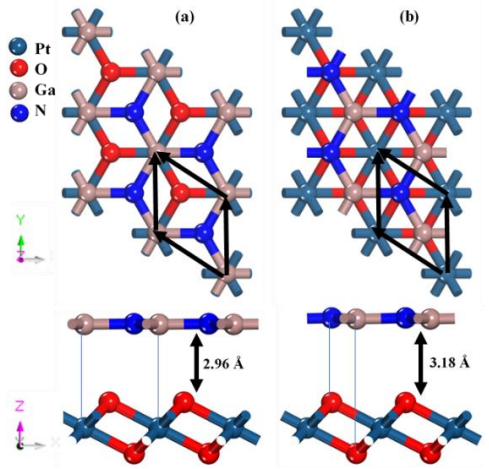

FIGURE 1. VdW stacked models for (a) HBL1, and (b) HBL6. The black solid lines are for the unit cell of the hetero-bilayer (HBL).

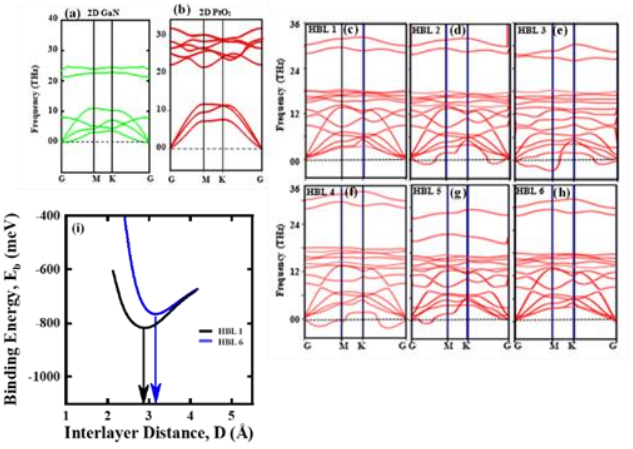

FIGURE 2. Phonon dispersion curves for (a) 2D GaN, (b) 2D PtO2, (c) HBL 1, (d) HBL 2, (e) HBL 3, (f) HBL 4, (g) HBL 5, and (h) HBL 6, and (i) interlayer binding energy curves.

and O_l atoms, respectively; in HBL 2, N (Ga) atoms are right on the Pt (O_l) atoms; In HBL 3, Ga atoms are stacked on the Pt atoms and N atoms are on the top of O_u; In HBL 4, N (Ga) atoms are stacked on top of Pt (O_u) atoms; In HBL 5, Ga (N) atoms are directly on top of O_l (O_u) atoms; finally, in HBL 6, the order is reversed i.e., N (Ga) atoms are straight on top of O_l (O_u) atoms. The geometry relaxed structures of the HBLs (HBL 1, and HBL 6) are shown in **Fig 1 (a), and (b). Figure 2** shows the phonon dispersion curves for 2D GaN **(a)**, 2D PtO_2 **(b)**, HBL 1 **(c)**, HBL 2 **(d)**, HBL 3 **(e)**, HBL 4 **(f)**, HBL 5 **(g)**, and HBL 6 **(h)**, including the interlayer binding energy curves **(i)**. The dynamic stability test is done on the HBLs through density functional perturbation theory (DFPT) and the HBL 1 (**Fig.2(a)**), and HBL 6 (**Fig.2(h)**) are found dynamically stable. The other HBLs, HBL 2, HBL3, HBL4, HBL 5 are dynamically unstable as negative phonon branches are found in the phonon dispersion curves as depicted in **Figs. 2(d - g).** We have also excluded the unstable HBLs from our further studies. The dynamically stable optimized HBLs have lattice constants ~3.209 Å (~3.208) Å for HBL 1 (HBL 6), which also remains in the lattice constant range of 2D GaN and 2D PtO_2, as expected as in the theory. Among the HBLs, HBL 1 (HBL 6) has the smallest (highest) interlayer spacing ~ 2.963 Å (~ 3.180 Å).

To reveal the exothermic feasibility of the HBLs, the interlayer spacing dependent binding energy is calculated by the following equation,

$$E_b = E_{GaN/PtO2\ HBL} - E_{GaN} - E_{PtO2} \quad (5)$$

where, $E_{GaN/PtO2\ HBL}$ = dispersion corrected total energy of the HBL, E_{GaN} = the energy of 2D GaN and E_{PtO2} = the total energy of 2D PtO_2. The binding energy curves are shown in **Fig.2 (i).** The binding energies, respective interlayer distances, optimized lattice constants, and buckling heights, bond lengths are enlisted in **TABLE II**. The binding energy predicts the most energetically favorable HBL and HBL 1 is the most favorable. As strong binding energy means strong interlayer coupling in the HBLs, the HBL 1 has the smallest interlayer spacing with the highest cross-layer coupling. These cross-layer spacing variations appear due to the atomic orientation while stacking. Now, to evaluate whether the HBLs are vdW bonded or covalent bonded, we have calculated the sum of vdW and covalent radii of the stacked atoms. The smallest cross-layer spacing is ~2.963 Å in HBL 1, higher than the accumulation of covalent radii of Ga (1.26 Å) and Pt (1.3 Å) atom i.e., 2.56 Å, indicating the absence of covalent bonding between the 2D layers. However, the cross-layer distance is within the accumulated vdW radii of Ga (1.87 Å) and Pt (1.75 Å) atom i.e., 3.62 Å, referring to the existence of vdW interaction in between the stacked layers.

TABLE II

OPTIMIZED a (Å), BOND LENGTH dB (Å), BUCKLING HEIGHT, d_H (Å), CROSS-LAYER BINDING ENERGY, E_b (meV), CROSS-LAYER SPACING, D (Å), BANDGAP E_g^{PBE} (eV) USING GGA-PBE FUNCTIONAL, BANDGAP $E_g^{HSE\ 06}$(eV) USING HSE-06 NON-LOCAL FUNCTIONAL, AND BANDGAP E_g^{MGGA}(eV) USING META-GGA (MGGA) FUNCTIONAL WITH 2D PRHG.

Structure	a (Å)	d_B (Å)	d_H (Å)	E_b (meV)	D (Å)	E_g^{PBE} (eV)	$E_g^{HSE\ 06}$ (eV)	E_g^{MGGA} (eV)
2D GaN	3.248	1.875	0.0	-	-	2.29 K/G	3.42 K/G	4.291 K/G
2D PtO_2	3.168	2.07	1.865			1.90 G/M*	3.57 G/M*	4.847 G/M*
HBL 1	3.209	-	-	-820	2.963	0.42 K /M*	1.04 K /M*	2.650 K /M*
HBL 6	3.208	-	-	-770	3.180	0.49 K /M*	1.08 K /M*	2.690 K /M*

This article has been accepted for publication in a future issue of this journal, but has not been fully edited. Content may change prior to final publication. Citation information: DOI 10.1109/ACCESS.2021.3102190, IEEE Access

B. ELECTRONIC PROPERTIES OF HETERO-BILAYER SYSTEM

To implement our user-defined meta-GGA (MGGA) for the rest of the electronic properties, we have evaluated the functional by comparing with experimental value and quasiparticle (QP) GW bandgap value. The comparison of GGA-PBE, HSE 06, GW, and experimental bandgap with customized MGGA (2D PRHG with 2D corrected PBE) is depicted along with the band structures in **Fig. 3 (a)-(d), (i)**. The bandgap values we have calculated using various functionals are in correspondence with the other theoretical and experimental studies. The wonder is that the customized MGGA well-predicts the bandgap with acceptable accuracy as compared with the GW bandgap (~5% deviation from GW in 2D GaN) and experimental (our proposed MGGA underestimates 2D GaN bandgap ~0.82 eV while GW approximation underestimates the bandgap ~1.04 eV). These comparisons suggest that the customized MGGA is well-suited for almost ~90% reducing of computational cost within acceptable accuracy (e.g., GW requires 64 CPU hours while MGGA requires only 2 CPU hours for the same type of calculations). The MGGA band structures of the HBLs are also depicted in **Fig. 3 (e)-(h)**. As depicted, the bandgap values are highly receptive in the value due to stacking. The HBL 1 and HBL 6 both have indirect bandgap with almost ~2 times lowering of the bandgap values from their constituents, facilitating for the PWS application.

To evaluate the photocatalytic water splitting activity of the VdW HBL, the relative band edges are to be calculated. For this purpose, the MGGA bandgap values are considered utilizing the equation $E_{CB} = X - E_e - (\frac{E_g^{MGGA}}{2})$ for conduction band edge (CBE) and $E_{VB} = X - E_e + (\frac{E_g^{MGGA}}{2})$ for valance band edge (VBE) calculation. Where, the Mulliken electronegativities of the comprising atoms of the hetero-bilayers are denoted by X, E_e represents the standard hydrogen

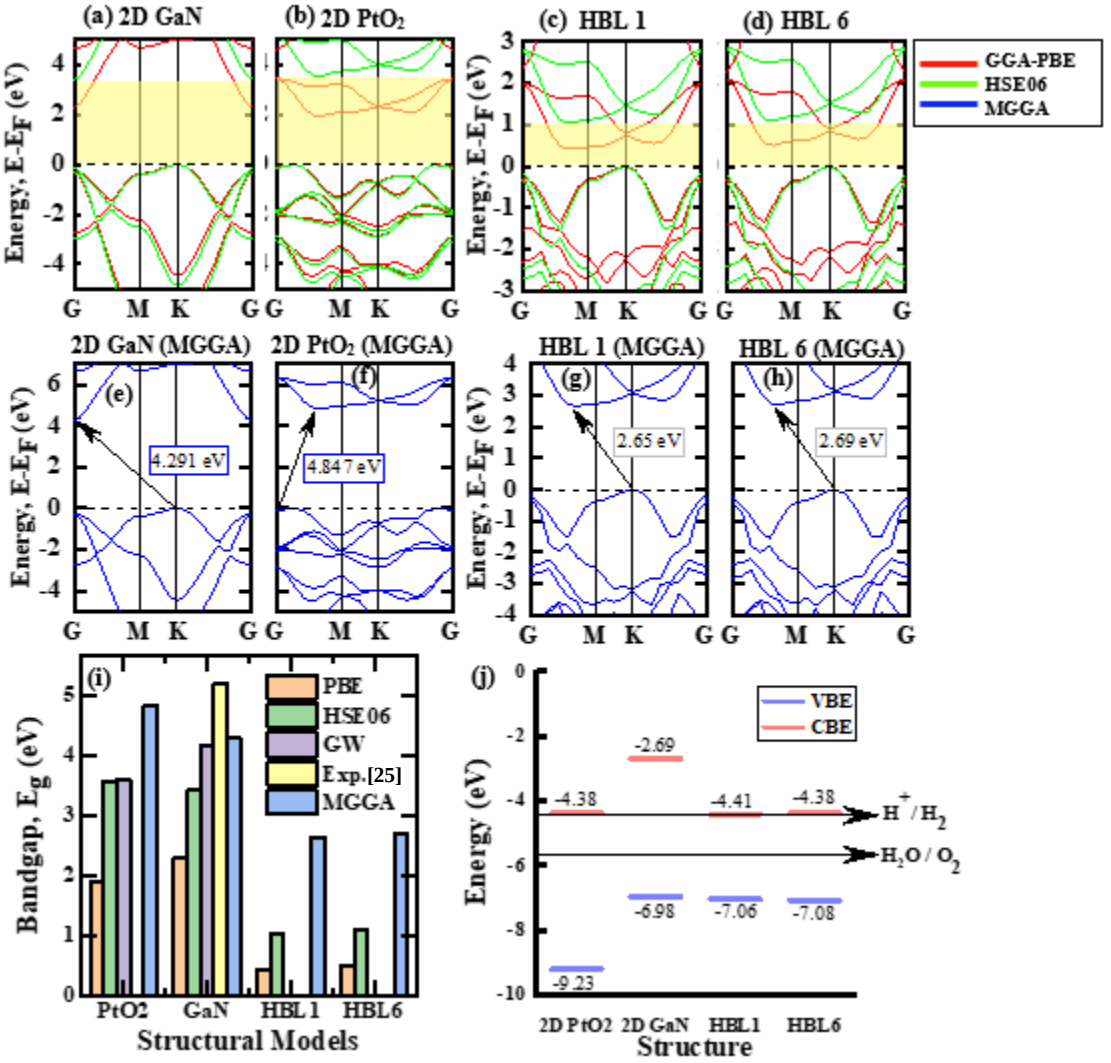

FIGURE 3. The band-structures calculated by GGA-PBE, and HSE06 for (a) 2D GaN), (b) 2D PtO_2, (c) HBL 1, (d) HBL 6. The band structures calculated by customized MGGA functional for (e) 2D GaN), (f) 2D PtO_2, (g) HBL 1, (h) HBL 6. (i) Comparative bandgap values. (j) Relative band alignment for 2D GaN, 2D PtO_2, HBL1, and HBL6 for photocatalytic water splitting.

potential (4.45 eV). The Mulliken electronegativity for 2D GaN (PtO_2) is 4.83 eV (6.80 eV). **Fig 3 (j)** demonstrates the VBE and CBE for the 2D GaN, 2D PtO_2, HBL 1, and HBL 6. The relative band-edge positions suggest that VBE is contributed by 2D GaN, and CBE contributed by 2D PtO_2, outlining the type-II band edge (staggering). At, pH level zero, the standard potential with respect to vacuum for ($2H^+/H_2$) reduction and (H_2O/O_2) oxidation potentials are at -4.46 eV, and -5.67 eV energy levels, respectively. In comparison with these reference values, both HBL 1 and HBL 6 have adequate kinetic overpotential for initiating the reduction and oxidation (redox) reactions, facilitating the hydrolysis potentiality. Moreover, the valance band offset (VBO) (conduction band offset (CBO)) is ~2.25 eV (1.69 eV), high enough to separate the carrier spatially. This high-VBO and CBO thus facilitates the potentiality of the photocatalysis of the water.

For the deep insights, we have evaluated the atomic orbital projected density of states (PDOS) (as shown in **Fig. 4 (a), and (b)**) so that the band-edge contributing atoms and their orbitals can be revealed. In both HBLs, the CBE is mainly subsidized by the d-orbital of Pt atom of the 2D PtO_2 layer, and the VBE is dominantly donated by p-orbital of N atom of the 2D GaN layer, marking the type-II (staggering) band positions. This finding is also theoretically in line with the relative band-edge calculation mentioned in the previous paragraph.

To gain the insights of charge transfer and contributing layers, the charge density difference is shown using, $\Delta\rho = \rho_{HBLs} - \rho_{2D\ PtO2} - P_{2D\ GaN}$, where, ρ_{HBLs} is the charge density of HBL, $\rho_{2D\ PtO2}$ is the charge density of 2D PtO_2 and $P_{2D\ GaN}$ is the charge density of the 2D GaN. The yellow (green) region refers to the charge depletion (accumulation). In both HBL (**Fig 5. (a), (b)**), N (O) predominantly depletes (accumulates) the charges. This nature signifies the charge transfer direction from N atoms of 2D GaN to O atoms of 2D PtO_2. The transfer is also confirmed by the comparative electro-negativities of the atom. As, the O atoms (~3.44) have higher electro-negativity than N atoms (~3.04), resulting in the charge transfer from N to O direction.

To find out the effective carrier separation capability, the spatial effective average potential along the cross-plane direction is calculated from the Poison equation. It turns out that 2D PtO_2 has a higher potential than 2D GaN which is reliable with the charge transmission as well. A significant amount of effective potential difference ~ 3.25 V is found. A strong electrostatic electric field arises due to the high-potential difference which results in spatially discretizing the charge carriers, operating as anti-recombinant, highly suggestive for photocatalysis applications. To proceed further, we have calculated the electron and hole effective masses of the HBLs and comprising 2D layer from dispersion band theory as summarized in **TABLE III**. The values reveal that the electron and hole effective masses are highly responsive to the stacking orientation of the HBLs. However, the HBLs show a low value of effective masses compared with their constituents, suggesting high-carrier mobility in the HBLs. Moreover, effective carrier separation is also suggestive due to the low recombination time as mobility is higher, also confirming the potential of spatial carrier separation and facilitating the PWS.

TABLE III

CALCULATED EFFECTIVE MASS m_e^*/m_0

Structure	m_e^*/m_0	m_h^*/m_0
2D GaN	0.467	1.018
2D PtO2	0.902	1.782
HBL 1	0.844	1.612
HBL 6	0.782	1.335

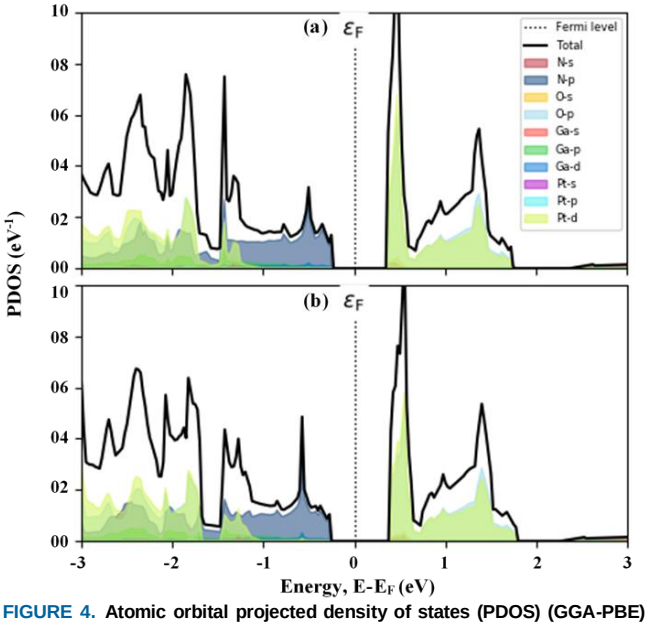

FIGURE 4. Atomic orbital projected density of states (PDOS) (GGA-PBE) for (a) HBL 1, and (b) HBL 6.

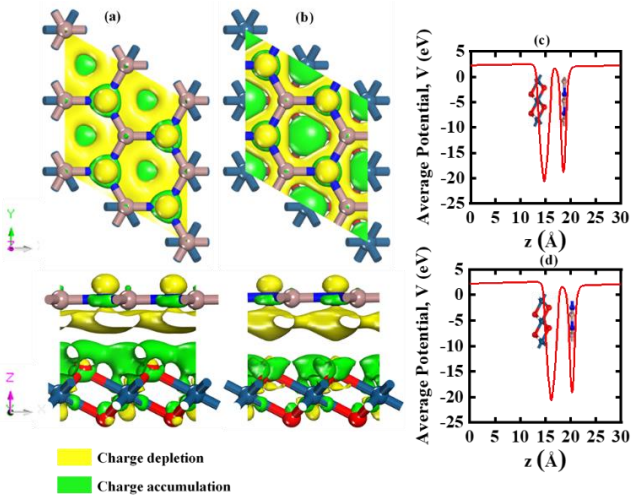

FIGURE 5. The charge density differences plot for (a) HBL 1, and (b) HBL 6. The yellow (green) color represents the charge depletion (accumulation). The iso value is assumed ~0.001 e Å^{-3}. Effective average potential differences for (c) HBL 1, and (d) HBL 6 are shown by red solid lines concerning the z-axis.

C. ELECTRONIC PROPERTIES OF HBLS: BIAXIAL STRAIN CONTRIBUTION

Biaxial strain, an intrinsic feature of vdW stacked HBL, arisen from the lattice mismatch is used here to alter the electronic properties. The biaxial strain tuned band structures for HBL l and HBL 6 are shown in **Fig. 6 (a), (b).** Unstrained HBL 1 shows an indirect bandgap ~ 2.65 eV at K (VBM) to M* (CBM). With increasing the compressive strains, the bands at the K point become lower and at the gamma (G) point pushed up, resulting in the bandgap increment from ~2.65 eV to 2.82 eV at 4% compressive strain. Simultaneously, the conduction band minima (CBM) are shifted toward the G point and pushed down due to the application of compressive strains. This trends also lower the bandgap value at 6% compressive strain and the bandgap becomes ~2.71 while at 4% compressive strain it is ~2.82 eV. Tensile strains, on the other hand, push up the band near the K point in the VBM and shift the band in the CBM from M* to M, resulting in the bandgap lowering with the increase of tensile strains. As a whole, both compressive and tensile strains seem to lower the bandgap value. In HBL 6, a similar fashion is observed with compressive and tensile strains. However, the highest bandgap is attained ~2.87 eV at 4% compressive strain.

To evaluate the band edge tunability due to the biaxial strain, we have calculated the CBE and VBE upon applying biaxial strains as depicted in **Fig 7 (a), (b)**. It is found that the HBL 1 has sufficient photocatalytic overpotential (P.O) up until 4% tensile strain. It has sufficient P.O from 6% compressive to 4% tensile strains. The highest P.O is attained at 4% compressive strain, and the overpotential for hydrogen evolution reaction (HER) is ~0.13 eV, and that for oxygen evolution reaction (OER) is ~1.47 eV. Conversely, the HBL6 has sufficient P.O in all the biaxial strains either compressive or tensile in the 6% compressive to 6 % tensile strains range. Again, the highest P.O is achieved at 4% compressive strain and the potential for HER (OER) is ~0.15 eV (1.50 eV). Interestingly, 4% compressive strain the P.O, facilitating the visible-light-driven PWS.

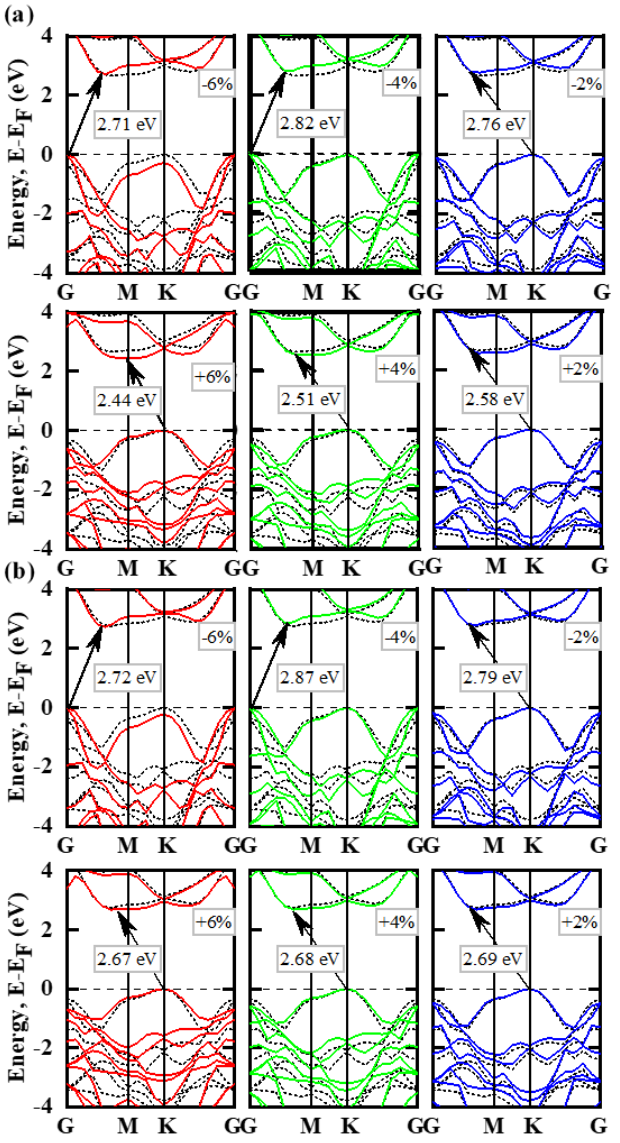

FIGURE 6. **Biaxial strain-tuned band structures upon 6% compressive to 6% tensile strain range for (a) HBL 1, and (b) HBL 6. Dotted lines show unstrained bands and solid lines represent strained bands.**

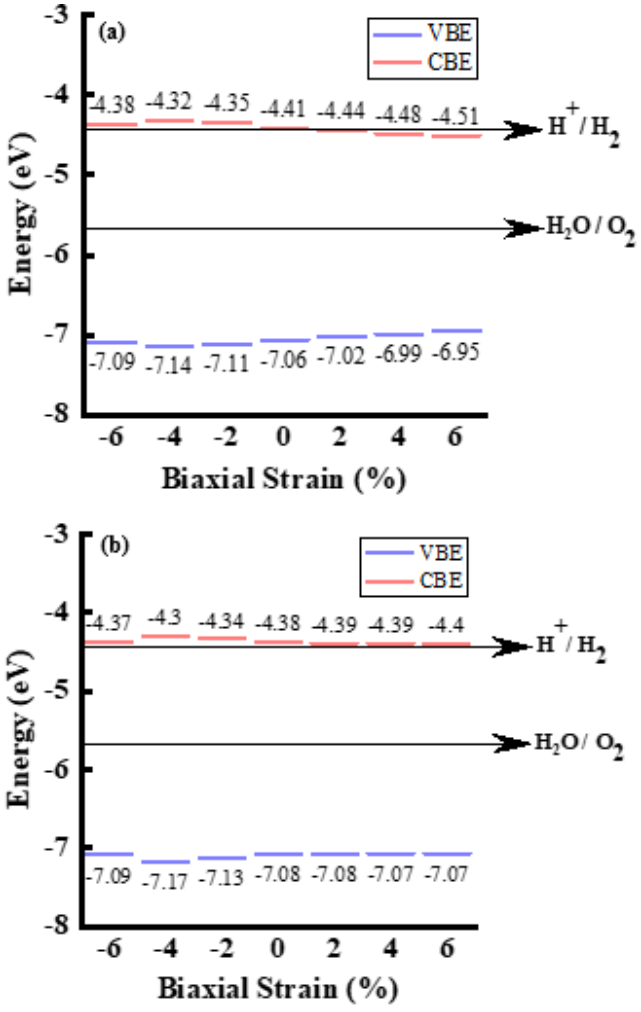

FIGURE 7. **Photocatalytic overpotential (P.O) with relative band positions for (a) HBL 1, and (b) HBL 6.**

This article has been accepted for publication in a future issue of this journal, but has not been fully edited. Content may change prior to final publication. Citation information: DOI 10.1109/ACCESS.2021.3102190, IEEE Access

D. OPTICAL PROPERTIES AND ITS TUNABILITY UPON BIAXIAL STRAINS

Exploring optical properties and tunability of it is significant to evaluate the key performance of photocatalysts. To do so, we have calculated the core optical properties namely, real and imaginary part of the dielectric function, absorption coefficients, and reflectivity using density functional theory (DFT). The complex and imaginary part of the dielectric functions is calculated for 0 eV to 15 eV of photon energy range as demonstrated in **Fig. 8 (a), (b).** Amazingly, no negative portion is found within the energy range in the real part of the dielectric function, revealing the semiconducting nature of the HBLs in the energy range. This property signifies the high refraction of light through the HBLs, suggesting higher photocurrent in the HBLs. The imaginary part of the dielectric function shows the nature of the peak in the HBLs. The first peaks are also depicted in the imaginary part of the dielectric function is shown in **Fig. 8 (b)**. The first peaks are at ~1.8 eV, and ~2.01 eV for HBL 1, and HBL 6, respectively, denoting the exciton energy of the materials. Both the parts of the dielectric function follow the trend of the dielectric function of 2D PtO_2 in a red-shifted manner, suggesting a strong influence on the HBL's optical property of the substrate material. Static dielectric constant, signifying electric field supporting capability, is also calculated for the HBLs and the constituent 2D layer and the HBLs show higher value compared with the constituents. The values are as following: In HBL 1 ~2.74, in HBL 6 ~2.5, in 2D PtO_2 ~ 1.8, and in 2D GaN ~1.45. Clearly, a ~1.89 times increment of the static dielectric function value upon stacking of the layer, which indicates a significant amount of photo-induced charge supporting capability.

The optical absorption coefficient is also calculated with respect to photon wavelength which signifies the photon conversion efficacy. In our proposed HBLs, ~10^6 cm^{-1} of absorption coefficient, 10 times greater than the perovskite materials, is attained at the ultra-violet (UV) photon wavelength, suggesting the material's high-absorption capability of photons [48], [49]. The absorption peaks again follow the trends of 2D PtO_2 in a red-shifted way. The gray lines in the **Fig. 8(c), (d)** represents solar flux (spectral irradiance), adopted in the curves for pointing out the spectrum range utilizes the most of the solar flux. It turns out that visible and near infrared (NIR) hold most of the solar irradiances. The absorption coefficients and reflectivity values calculated in our work, hence compared and commented with the flux value so that the optical performance improvements of the material can be revealed.

Surprisingly, though both comprising 2D layers have zero absorption coefficient in the visible spectrum, the HBLs have ~ 2×10^5 (at 380 nm) of absorption coefficient, highly recommended for PWS application. To proceed further, the reflectivity of the HBLs is calculated and the highest reflectivity is ~7% (at 407 nm) in the visible spectrum, significantly low, suggesting the low-loss nature of the materials. These high-absorption and low-reflectivity in the visible spectrum for the HBLs suggest the visible-light-driven PWS capability of the material, as well.

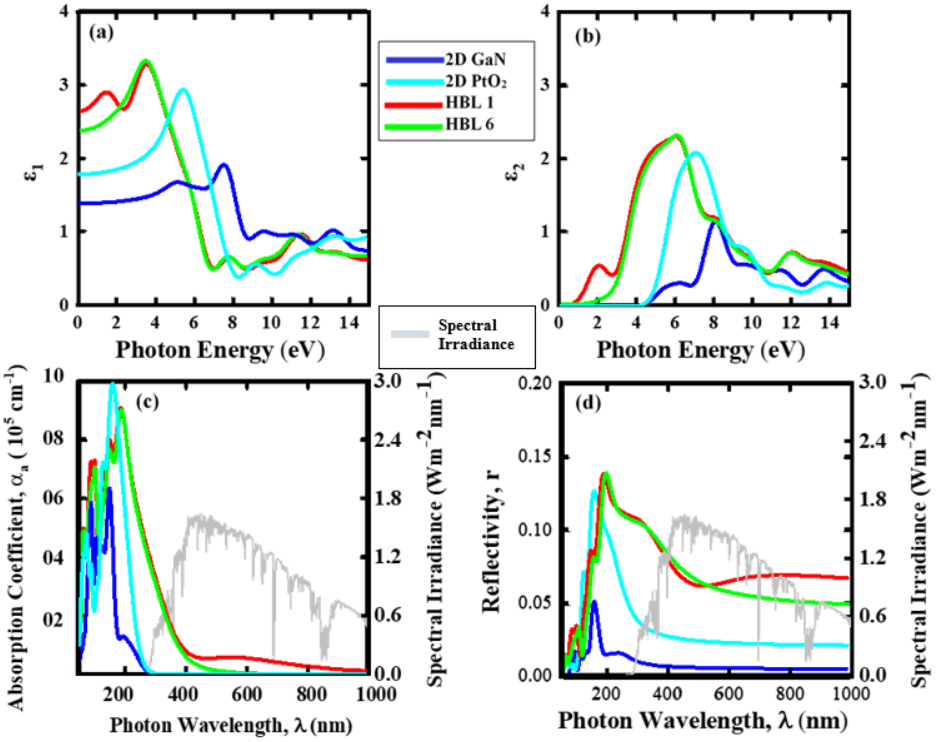

FIGURE 8. Photon energy-dependent (a) real dielectric function (b) imaginary dielectric function, and photon wavelength-dependent (c) absorption coefficient for intrinsic, (d) reflectivity of the HBL systems.

To find the further visible shifting of the absorption coefficients, we have calculated the biaxial strain-dependent absorption coefficients with respect to photo wavelength. The biaxial strain tuned absorption coefficients are shown in **Fig 9 (a), (b)**. In HBL 1, the unstrained absorption peak ~9×10^5 cm^{-1} is at 210 nm in the UV range and in the visible range it is 2×10^5 cm^{-1}. Upon applying compressive strains from -2% to -6%, the absorption coefficients are shifted towards the UV spectrum. Interestingly, due to the tensile strains ranges from 2% to +6%, the absorption coefficient is increased by almost ~2 times in the visible spectrum (from 290 nm to 400 nm), significant for the PWS application. The highest absorption peak achieved in the visible spectrum for HBL 1 is ~ 4.1×10^5 cm^{-1}, comparable to perovskite materials. In the HBL 6, the same phenomenon is observed for the absorption co-efficient, precisely, at 6% of tensile strain, the absorption peaks in the visible region appear almost ~2.1 times more compared with the unstrained condition, emulating high-photocatalytic carrier generations. In the visible spectrum for HBL 6, the tensile strain tuned absorption becomes as high as ~ 4.2×10^5 cm^{-1}, predicting enhanced carrier generation probability

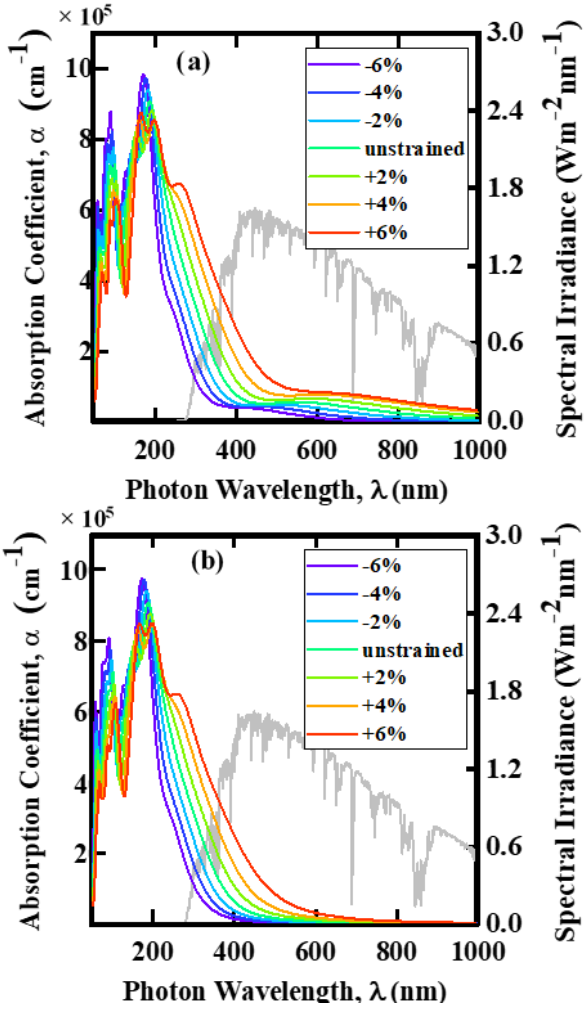

FIGURE 9. **Biaxial strain-tuned absorption coefficient for (a) HBL 1, and (b) HBL 6. Spectral irradiance is denoted by gray line.**

of HBL 6 compared with HBL 1. Interestingly, in both HBLs, for 6% tensile strain, another absorption peak is arisen at ~300 nm. This peak is due to the extra inter-band transition states originated by the proximal transition of CBM from M^* to M and the bandgap lowering. These values also suggest that within the permissible bandgap and P.O range, tensile strains in the HBL6 are more advantageous than in the HBL 1.

Concisely, the key performance factors of a photocatalysts are namely, the highest obtained bandgap, E_g, the highest optical absorption attained in the visible spectrum at a specific wavelength, α_s, reflectivity, r, photocatalytic overpotential (P.O), conduction band offset (CBO), and valance band offset (VBO) are summarized in the **TABLE IV** for benchmarking of this PtO_2/GaN with other 2D GaN (2D PtO_2) based vdW HBLs. These values also suggest that the PtO_2/GaN vdW HBLs can be more potential compared with their constituent layer based vdW HBLs.

IV. CONCLUSION

Harnessing first-principles density functional theory (DFT), we have explored the novel GaN/PtO_2 vdW HBL and its electronic, optical, and photocatalytic water splitting (PWS) capability. Two HBLs, HBL 1, and HBL 6 are found dynamically stable confirmed by phonon dispersion curves. Among them, the HBL 1 shows the lowest binding energy (~ 820 meV), suggesting the chemical formation feasibility of the vdW stacking. Both HBLs show visible ranged type-II bandgap. The bandgap becomes biaxial strains responsive in a manner that for both compressive and tensile strain, it tends to lower. However, some anomaly is found at 4% compressive strains due to the CBM-VBM shifting, forming the highest bandgap at this strain (~ 2.82 eV for HBL 1, and ~2.87 eV for HBL 6). The low-effective masses and interlayer effective potential show the spatial carrier separation probability of the HBL. Both the HBLs have sufficient photocatalytic overpotential (P.O) for the HER and OER. The overpotentials are also responsive to the biaxial strains and HBL 1 has the permissible strain range is -6 % to +4 % while for HBL 6 it is -6% to + 6%. The optical absorption coefficient in the visible spectrum is ~2×10^5 cm^{-1} (at ~380 nm) and the value can be further improved by ~2 (at ~383 nm) times upon applying 6% tensile strain, suggesting visible-light-driven PWS capability. Concisely, the visible ranged type-II bandgap, spatial carrier separation capability, improved visible ranged absorption coefficient and tunability of the properties suggest that the novel GaN/PtO_2 VdW HBL can be a potential visible-light-driven photocatalysts candidate, fulfilling almost all the PWS attributes.

ACKNOWLEDGMENT

This work was supported by the Deanship of Scientific Research (DSR), King Abdulaziz University, Jeddah, under grant No. DF 755-135-1441. The authors, therefore, gratefully acknowledge DSR technical and financial support.

TABLE IV

BENCHMARKING FOR PtO_2/GaN WITH 2D GaN (2D PtO_2) BASED VdW HBLS

VdW HBLs	E_g (eV)	α_s (cm^{-1})	r (%)	P.O (eV)	CBO (eV)	VBO (eV)
ZnO/GaN [35]	2.82	9×10^4	-	1.2 (HER) 0.33 (OER)	0.2	0.61
GaN/GeC [15]	3.47	10^5	-	0.9 (HER) 1.23 (OER)	0.06	0.97
GaN/MoSe2 [31]	1.7	2.1×10^5		-	2.8	0.34
GaN/BAs [28]	1.71	3.1×10^4	12	-	-	-
MoSSe/GaN [29]	1.5	3.9×10^5	-	-	1.48	0.37
PtO_2/MoS_2 [20]	1.5	10^5	-	-	-	-
PtO_2/GaN [This work]	**2.69**	**4.1×10^5**	**7**	**0.15 (HER) 1.5 (OER)**	**1.69**	**2.25**

P.O. = Photocatalytic overpotential, HER = Hydrogen evolution reaction, OER = Oxygen evolution reaction

REFERENCES

[1] H. T. Pao and C. M. Tsai, "CO2 emissions, energy consumption and economic growth in BRIC countries," *Energy Policy*, vol. 38, no. 12, pp. 7850–7860, 2010, doi: 10.1016/j.enpol.2010.08.045.

[2] D. Dodman, "Blaming cities for climate change? An analysis of urban greenhouse gas emissions inventories," *Environ. Urban.*, vol. 21, no. 1, pp. 185–201, 2009, doi: 10.1177/0956247809103016.

[3] S. J. Davis and K. Caldeira, "Consumption-based accounting of CO2 emissions," *Proc. Natl. Acad. Sci. U. S. A.*, vol. 107, no. 12, pp. 5687–5692, 2010, doi: 10.1073/pnas.0906974107.

[4] G. L. Chiarello, M. H. Aguirre, and E. Selli, "Hydrogen production by photocatalytic steam reforming of methanol on noble metal-modified TiO2," *J. Catal.*, vol. 273, no. 2, pp. 182–190, 2010, doi: 10.1016/j.jcat.2010.05.012.

[5] T. Jafari, E. Moharreri, A. S. Amin, R. Miao, W. Song, and S. L. Suib, "Photocatalytic water splitting - The untamed dream: A review of recent advances," *Molecules*, vol. 21, no. 7, 2016, doi: 10.3390/molecules21070900.

[6] S. Czernik, R. Evans, and R. French, "Hydrogen from biomass-production by steam reforming of biomass pyrolysis oil," *Catal. Today*, vol. 129, no. 3–4, pp. 265–268, 2007, doi: 10.1016/j.cattod.2006.08.071.

[7] J. M. Macak, M. Zlamal, J. Krysa, and P. Schmuki, "Self-organized TiO2 nanotube layers as highly efficient photocatalysts," *Small*, vol. 3, no. 2, pp. 300–304, 2007, doi: 10.1002/smll.200600426.

[8] U. Maitra, U. Gupta, M. De, R. Datta, A. Govindaraj, and C. N. R. Rao, "Highly effective visible-light-induced H2 generation by single-layer 1T-MoS2 and a nanocomposite of few-layer 2H-MoS 2 with heavily nitrogenated graphene," *Angew. Chemie - Int. Ed.*, vol. 52, no. 49, pp. 13057–13061, 2013, doi: 10.1002/anie.201306918.

[9] C. N. R. Rao *et al.*, "Superlattices of covalently cross-linked 2D materials for the hydrogen evolution reaction," *APL Mater.*, vol. 8, no. 2, 2020, doi: 10.1063/1.5135340.

[10] J. Zhang, P. Zhou, J. Liu, and J. Yu, "New understanding of the difference of photocatalytic activity among anatase, rutile and brookite TiO2," *Phys. Chem. Chem. Phys.*, vol. 16, no. 38, pp. 20382–20386, 2014, doi: 10.1039/c4cp02201g.

[11] J. Ran, W. Guo, H. Wang, B. Zhu, J. Yu, and S. Z. Qiao, "Metal-Free 2D/2D Phosphorene/g-C3N4 Van der Waals Heterojunction for Highly Enhanced Visible-Light Photocatalytic H2 Production," *Adv. Mater.*, vol. 30, no. 25, pp. 2–7, 2018, doi: 10.1002/adma.201800128.

[12] A. Di Bartolomeo, "Emerging 2d materials and their van der waals heterostructures," *Nanomaterials*, vol. 10, no. 3, pp. 1–10, 2020, doi: 10.3390/nano10030579.

[13] R. Zhang, L. Zhang, Q. Zheng, P. Gao, J. Zhao, and J. Yang, "Direct Z-Scheme Water Splitting Photocatalyst Based on Two-Dimensional Van der Waals Heterostructures," *J. Phys. Chem. Lett.*, vol. 9, no. 18, pp. 5419–5424, 2018, doi: 10.1021/acs.jpclett.8b02369.

[14] Md. Sakib Hasan Khan, Md. Rafiqul Islam, and Md. Tanvir Hasan, "Strain-dependent electronic and optical properties of boron-phosphide and germanium-carbide hetero-bilayer: A first-principles study," vol. 085128, 2020, doi: 10.1063/5.0021359.

[15] Md. Sakib Hasan Khan, Md. Rafiqul Islam, Muhammad Shaffatul Islam, Ibrahim M. Mehedi, and Md. Tanvir Hasan, "Tunable Photocatalytic Properties of Planar GaN/GeC Hetero-bilayer: Production of H2 Fuel," *IEEE Access*, p. 1, 2020, doi: 10.1109/ACCESS.2020.3037036.

[16] A. K. Singh, K. Mathew, H. L. Zhuang, and R. G. Hennig, "Computational screening of 2D materials for photocatalysis," *J. Phys. Chem. Lett.*, vol. 6, no. 6, pp. 1087–1098, 2015, doi: 10.1021/jz502646d.

[17] T. Yang *et al.*, "Atomically Thin 2D Transition Metal Oxides: Structural Reconstruction, Interaction with Substrates, and Potential Applications," *Adv. Mater. Interfaces*, vol. 6, no. 1, pp. 1–19, 2019, doi: 10.1002/admi.201801160.

[18] J. Zhang, Y. Xie, Y. Hu, and H. Shao, "Remarkable intrinsic ZT in the 2D PtX2(X = O, S, Se, Te) monolayers at room temperature," *Appl. Surf. Sci.*, vol. 532, no. May, p. 147387, 2020, doi: 10.1016/j.apsusc.2020.147387.

[19] A. Shokri, A. Yazdani, and K. Rahimi, "Tunable electronic and optical properties of g-ZnO/α-PtO2 van der Waals heterostructure: A density functional theory study," *Mater. Chem. Phys.*, vol. 255, no. July, p. 123617, 2020, doi: 10.1016/j.matchemphys.2020.123617.

[20] J. Li and S. Y. Xie, "van der Waals PtO2/MoS2 heterostructure verified from first principles," *Phys. Lett. Sect. A Gen. At. Solid State Phys.*, vol. 384, no. 14, pp. 8–11, 2020, doi: 10.1016/j.physleta.2020.126286.

[21] L. Xie *et al.*, "A Ni(OH)2-PtO2 hybrid nanosheet array with ultralow Pt loading toward efficient and durable alkaline hydrogen evolution," *J. Mater. Chem. A*, vol. 6, no. 5, pp. 1967–1970, 2018, doi: 10.1039/c7ta09990h.

[22] Z. Wang *et al.*, "Ultrafine PtO2 nanoparticles coupled with a Co(OH)F nanowire array for enhanced hydrogen evolution," *Chem. Commun.*, vol. 54, no. 7, pp. 810–813, 2018, doi: 10.1039/c7cc08870a.

[23] G. Z. Wang, S. H. Dang, W. X. Zhao, Y. D. Li, S. Y. Xiao, and M. M. Zhong, "Tunable Photocatalytic Properties of GaN-Based Two-Dimensional Heterostructures," *Phys. Status Solidi Basic Res.*, vol. 255, no. 8, pp. 4–7, 2018, doi: 10.1002/pssb.201800133.

[24] C. Sun, M. Yang, T. Wang, Y. Shao, Y. Wu, and X. Hao, "Graphene-Oxide-Assisted Synthesis of GaN Nanosheets as a New Anode Material for Lithium-Ion Battery," *ACS Appl. Mater. Interfaces*, vol. 9, no. 32, pp. 26631–26636, 2017, doi: 10.1021/acsami.7b07277.

[25] Z. Y. Al Balushi *et al.*, "Two-dimensional gallium nitride realized via graphene encapsulation," *Nat. Mater.*, vol. 15, no. 11, pp. 1166–1171, 2016, doi: 10.1038/nmat4742.

[26] Q. Peng, C. Liang, W. Ji, and S. De, "Mechanical properties of g-GaN: A first principles study," *Appl. Phys. A Mater. Sci. Process.*, vol. 113, no. 2, pp. 483–490, 2013, doi: 10.1007/s00339-013-7551-4.

[27] B. Liu, W. Yang, J. Li, X. Zhang, P. Niu, and X. Jiang, "Template Approach to Crystalline GaN Nanosheets," *Nano Lett.*, vol. 17, no. 5, pp. 3195–3201, 2017, doi: 10.1021/acs.nanolett.7b00754.

[28] A. A. Attia and H. R. Jappor, "Tunable electronic and optical properties of new two-dimensional GaN/BAs van der Waals heterostructures with

the potential for photovoltaic applications," *Chem. Phys. Lett.*, vol. 728, no. April, pp. 124–131, 2019, doi: 10.1016/j.cplett.2019.05.005.

[29] K. Ren *et al.*, "High-efficiency photocatalyst for water splitting: A Janus MoSSe/XN (X = Ga, Al) van der Waals heterostructure," *J. Phys. D. Appl. Phys.*, vol. 53, no. 18, 2020, doi: 10.1088/1361-6463/ab71ad.

[30] K. Ren, Y. Luo, J. Yu, and W. Tang, "Theoretical prediction of two-dimensional ZnO/GaN van der Waals heterostructure as a photocatalyst for water splitting," *Chem. Phys.*, vol. 528, no. September 2019, p. 110539, 2020, doi: 10.1016/j.chemphys.2019.110539.

[31] Z. Cui *et al.*, "Electronic and optical properties of van der Waals heterostructures of g-GaN and transition metal dichalcogenides," *Appl. Surf. Sci.*, vol. 492, pp. 513–519, 2019, doi: 10.1016/j.apsusc.2019.06.207.

[32] M. Sun, J. P. Chou, J. Yu, and W. Tang, "Electronic properties of blue phosphorene/graphene and blue phosphorene/graphene-like gallium nitride heterostructures," *Phys. Chem. Chem. Phys.*, vol. 19, no. 26, pp. 17324–17330, 2017, doi: 10.1039/c7cp01852e.

[33] K. Ren *et al.*, "A van der Waals Heterostructure Based on Graphene-like Gallium Nitride and Boron Selenide: A High-Efficiency Photocatalyst for Water Splitting," *ACS Omega*, vol. 4, no. 26, pp. 21689–21697, 2019, doi: 10.1021/acsomega.9b02143.

[34] G. Wang *et al.*, "Rotation Tunable Photocatalytic Properties of ZnO/GaN Heterostructures," *Phys. Status Solidi Basic Res.*, vol. 257, no. 3, pp. 1–6, 2020, doi: 10.1002/pssb.201900663.

[35] G. Wang *et al.*, "Biaxial strain tunable photocatalytic properties of 2D ZnO/GeC heterostructure," *J. Phys. D. Appl. Phys.*, vol. 53, no. 1, pp. 0–6, 2020, doi: 10.1088/1361-6463/ab440e.

[36] A. Mogulkoc, Y. Mogulkoc, M. Modarresi, and B. Alkan, "Electronic structure and optical properties of novel monolayer gallium nitride and boron phosphide heterobilayers," *Phys. Chem. Chem. Phys.*, vol. 20, no. 44, pp. 28124–28134, 2018, doi: 10.1039/c8cp05529g.

[37] S. J. Clark *et al.*, "First principles methods using CASTEP," *Zeitschrift fur Krist.*, vol. 220, no. 5–6, pp. 567–570, 2005, doi: 10.1524/zkri.220.5.567.65075.

[38] J. P. Perdew, K. Burke, and M. Ernzerhof, "Generalized gradient approximation made simple," *Phys. Rev. Lett.*, vol. 77, no. 18, pp. 3865–3868, 1996, doi: 10.1103/PhysRevLett.77.3865.

[39] S. Grimme, "Semiempirical hybrid density functional with perturbative second-order correlation," *J. Chem. Phys.*, vol. 124, no. 3, 2006, doi: 10.1063/1.2148954.

[40] A. P. Bartók and J. R. Yates, "Regularized SCAN functional," *J. Chem. Phys.*, vol. 150, no. 16, pp. 1–6, 2019, doi: 10.1063/1.5094646.

[41] S. Grimme, "Accurate description of van der Waals complexes by density functional theory including empirical corrections," *J. Comput. Chem.*, vol. 25, no. 12, pp. 1463–1473, 2004, doi: 10.1002/jcc.20078.

[42] Md. Sakib Hasan Khan, Md. Rafiqul Islam, and Md. Tanvir Hasan, "Electronic and optical properties of BeO Co-doped 2D GaN using first-principles," *Proc. 2020 11th Int. Conf. Electr. Comput. Eng. ICECE 2020*, pp. 258–261, 2020, doi: 10.1109/ICECE51571.2020.9393143.

[43] Md. Sakib Hasan Khan, Farha Islam Mime, and Md. Rafiqul Islam, "Electronic and Optical Properties of Sn Doped Hexagonal BN Monolayer: A First-principles Study," *2020 IEEE Reg. 10 Symp. TENSYMP 2020*, no. June, pp. 230–233, 2020, doi: 10.1109/TENSYMP50017.2020.9230995.

[44] A. You, M. A. Y. Be, and I. In, "Band gap of β- PtO 2 from first-principles," *AIP Adv.*, vol. 022172, no. March, 2012.

[45] T. M. Pedersen, W. Xue Li, and B. Hammer, "Structure and activity of oxidized Pt(110) and α-PtO2," *Phys. Chem. Chem. Phys.*, vol. 8, no. 13, pp. 1566–1574, 2006, doi: 10.1039/b515166j.

[46] J. J. Blackstock, W. F. Stickle, C. L. Donley, D. R. Stewart, and R. S. Williams, "Internal structure of a molecular junction device: Chemical reduction of PtO2 by Ti evaporation onto an interceding organic monolayer," *J. Phys. Chem. C*, vol. 111, no. 1, pp. 16–20, 2007, doi: 10.1021/jp066266v.

[47] H. A. H. Mohammed, G. M. Dongho-Nguimdo, and D. P. Joubert, "Comprehensive first-principles study of bulk, bilayer, and monolayer α-PtO2 properties," *Phys. E Low-Dimensional Syst. Nanostructures*, vol. 127, p. 114514, 2021, doi: 10.1016/j.physe.2020.114514.

[48] P. Tonui, S. O. Oseni, G. Sharma, Q. Yan, and G. Tessema Mola, "Perovskites photovoltaic solar cells: An overview of current status," *Renew. Sustain. Energy Rev.*, vol. 91, no. April, pp. 1025–1044, 2018, doi: 10.1016/j.rser.2018.04.069.

[49] Partha Protim Mondal, Md. Sakib Hasan Khan, Md. Rafiqul Islam, and Md. Reivi Kaysir, "Performance Analysis of Perovskite Solar Cells with Different Structures," 2019, doi: 10.1109/ECACE.2019.8679329.